Chemical Science

ROYAL SOCIETY OF CHEMISTRY

EDGE ARTICLE

View Article Online
View Journal | View Issue

Cite this: *Chem. Sci.*, 2025, **16**, 22029

All publication charges for this article have been paid for by the Royal Society of Chemistry

Engineering Pd-based charge-asymmetrical metal pair sites to promote *CHO–CHO coupling for selective C_2 photoreduction to C_2H_4

Zhijie Pan,† Wenbin Liao,† Wenbiao Zhang, † Qun Liao, Mingyao Zhao, Xionghui Fu, Yuanming Zhang,* Yi Zhu * and Qingsheng Gao *

Received 17th July 2025
Accepted 8th October 2025

DOI: 10.1039/d5sc05310b

rsc.li/chemical-science

The photoreduction of CO_2 to C_{2+} products is primarily limited by the kinetic challenges of C–C coupling. Here, we engineer Pd-based charge-asymmetrical metal pair sites to accommodate the energetically favourable *CHO–CHO coupling pathway, accomplishing the excellent activity and selectivity toward C_2H_4. The as-designed Pd-loaded CdS nanospheres (Pd/CdS-Sv) featured Pd–Cd charge-asymmetrical sites co-manipulated by variable Pd loading and sulfur vacancies. They afford a C_2H_4 evolution rate as high as 14.2 μmol g^{-1} h^{-1}, with a selectivity of up to 81.6%, outperforming most reported photocatalysts. *In situ* diffuse reflectance infrared Fourier transform spectra distinctly identify the favourable *CHO–CHO coupling pathway on Pd/CdS-Sv, which benefits from the obviously shortened C–C bond of 1.453 Å on the Pd–Cd sites as compared to that in *CO dimerization (3.508 Å) according to theoretical calculations. The introduction of Pd promotes water dissociation and provides sufficient *H to enable the conversion of *CO to *CHO and more importantly lowers the energy barrier of the *CHO–CHO coupling on the charge-asymmetrical pair sites from 0.37 eV to −0.29 eV, thereby avoiding the sluggish *CO–CO dimerization. Gaining new insights into engineering charge-asymmetrical sites to effectively perform C–C coupling pathways, this work will expedite catalyst exploitation for CO_2 photoreduction.

Introduction

Excessive emissions of CO_2 are contributing to the severe greenhouse effect, and sunlight-driven conversion of CO_2 into valuable chemicals has been recognized as a viable approach to mitigating this crisis.[1–4] So far, existing catalysts are generally capable of photoconversion of CO_2 into C_1 products such as CO and CH_4; however, it is still tough to obtain C_2 products through solar-powered CO_2 reduction despite the excellent higher energy density and attractive economic value.[5,6] The C–C coupling of C_1 intermediates limits the C_2 production.[7,8]

To improve the efficiency toward C_2 products, various strategies have been developed, including optimizing crystal phases and morphologies, incorporating metal dopants,[9–12] introducing defects,[13] and creating heterostructures.[14] Recently, constructing charge-asymmetric active sites has emerged as a strategy of great potential to boost the C–C coupling of C_1 intermediates.[15,16] The different charge distributions of neighboring C_1 intermediates adsorbed on these charge-asymmetric active sites help suppress the electrostatic repulsion, which is beneficial for their self-coupling.[17,18] For example, Guo and co-workers[19] reported a dual-metal photocatalyst InCu/PCN for efficient ethanol production, which consists of atomically dispersed copper and indium loaded on polymeric carbon nitrides. Similarly, Shen and co-workers[20] designed nanocomposites composed of Au loaded on CeO_2 nanocrystals to enhance C_2H_6 formation. However, these ways of performing C–C coupling still encounter the high energy barrier of the *CO–CO pathway. Very recently, theoretical investigations have suggested that the pathway involving the hydrogenation of *CO to *CHO, followed by *CHO–CHO coupling, exhibits a lower kinetic energy barrier than the *CO–CO dimerization pathway. Specifically, Asthagiri and co-workers[21] revealed that the hydrogenation of *CO to *CHO followed by the dimerization of *CHO may be the primary mechanism for the generation of C_2H_4 on the Cu (100) surface at low potentials, rather than the previously hypothesized direct dimerization of *CO. Therefore, developing an effective strategy to both construct charge-asymmetric active sites and enable a favorable shift in the C–C coupling pathway is crucial for the photoreduction of CO_2 to valuable C_2 fuels.

CdS has emerged as a promising photocatalyst due to its narrow bandgap, high charge separation efficiency and appropriate conduction band potential.[22] Although extensive efforts have been devoted to adjusting intermediate adsorption and promoting photocatalytic CO_2 reduction on CdS-based photocatalysts through electronic modulation, they are typically limited to C_1 rather than C_2 production. It seems that mere

College of Chemistry and Materials Science, Jinan University, Guangzhou 510632, P. R. China. E-mail: tzhangym@jnu.edu.cn; tzhury@jnu.edu.cn; tqsgao@jnu.edu.cn

† These authors contributed equally to this work.

modulation of the electronic structure is difficult for C_2 generation. In this case, sulfur vacancies were introduced into CdS nanoparticles to induce structural relaxation and electronic structure modulation, and C_2H_4 could be produced with a low production rate (0.8 μmol g^{-1} h^{-1}) and selectivity (8.2%).[23] The symmetric Cd–Cd sites possess the same charge distribution near the sulfur vacancies, which leads to electrostatic repulsion and is detrimental to C–C coupling. Meanwhile, *H is not sufficiently generated for the conversion of *CO to *CHO to promote the energetically favorable *CHO–CHO coupling. Pd-based catalysts demonstrate significant potential in photocatalytic CO_2 reduction, as exemplified by the tandem system consisting of CdS@PCN-Co and Pd/PCN-Zn, which enables the efficient synthesis of high-value products such as pinacol and benzanilide *via* CO_2 photoreduction, while the composite photocatalyst $(Cu_1Pd_2)_x$@PCN-222(Co) achieves the photocatalytic conversion of CO_2 to benzophenone with high selectivity.[24,25] Introducing Pd to CdS can create charge-asymmetrical sites and provide sufficient *H simultaneously as Pd favors water dissociation, making it an ideal way of generating C_2 products.[26,27]

Herein, we have synthesized Pd-loaded CdS nanospheres with sulfur vacancies (*x*-Pd/CdS-Sv, *x* denotes the dosage of K_2PdCl_4), on which Pd–Cd charge-asymmetrical metal pair sites have been constructed to accommodate the energetically favourable *CHO–CHO coupling pathway. The optimal 1.5-Pd/CdS-Sv exhibited a C_2H_4 evolution rate of about 14.2 μmol g^{-1} h^{-1} with a selectivity as high as 81.6%, surpassing most previously reported photocatalysts under similar conditions. The favourable *CHO–CHO coupling pathway, rather than *CO dimerization, was clearly identified on the Pd–Cd charge-asymmetrical metal pair sites by using *in situ* diffuse reflectance infrared Fourier transform spectroscopy. Accordingly, theoretical studies pointed out the obviously shortened C–C bond of 1.453 Å for the *CHO–CHO coupling, as compared to that in *CO dimerization (3.508 Å). The introduction of Pd promoted water dissociation and provided sufficient *H to enable the conversion of *CO to *CHO, intentionally inducing the C–C coupling pathway from the kinetically sluggish *CO–CO to the fast *CHO–CHO pathways with an obviously reduced energy barrier.

Results and discussion

Structural and morphological characterization

As shown in the XRD pattern (Fig. 1a), CdS-Sv and *x*-Pd/CdS-Sv could be easily correlated to cubic CdS (JCPDS no. 65-2887). The peaks observed at $2\theta = 26.5°$, 43.9°, and 52.0° corresponded to the (111), (220), and (311) crystal planes of CdS.[23] The transmission electron microscopy (TEM) image of 1.5-Pd/CdS-Sv in Fig. 1b and the scanning electron microscopy (SEM) image of CdS-Sv in Fig. S1 showed that the CdS nanoparticles are spherical in shape. In the high-resolution TEM (HRTEM) image (Fig. 1c), the lattice fringe spacing of 0.33 nm was assigned to the (111) crystal planes of cubic CdS,[23] and the lattice fringe

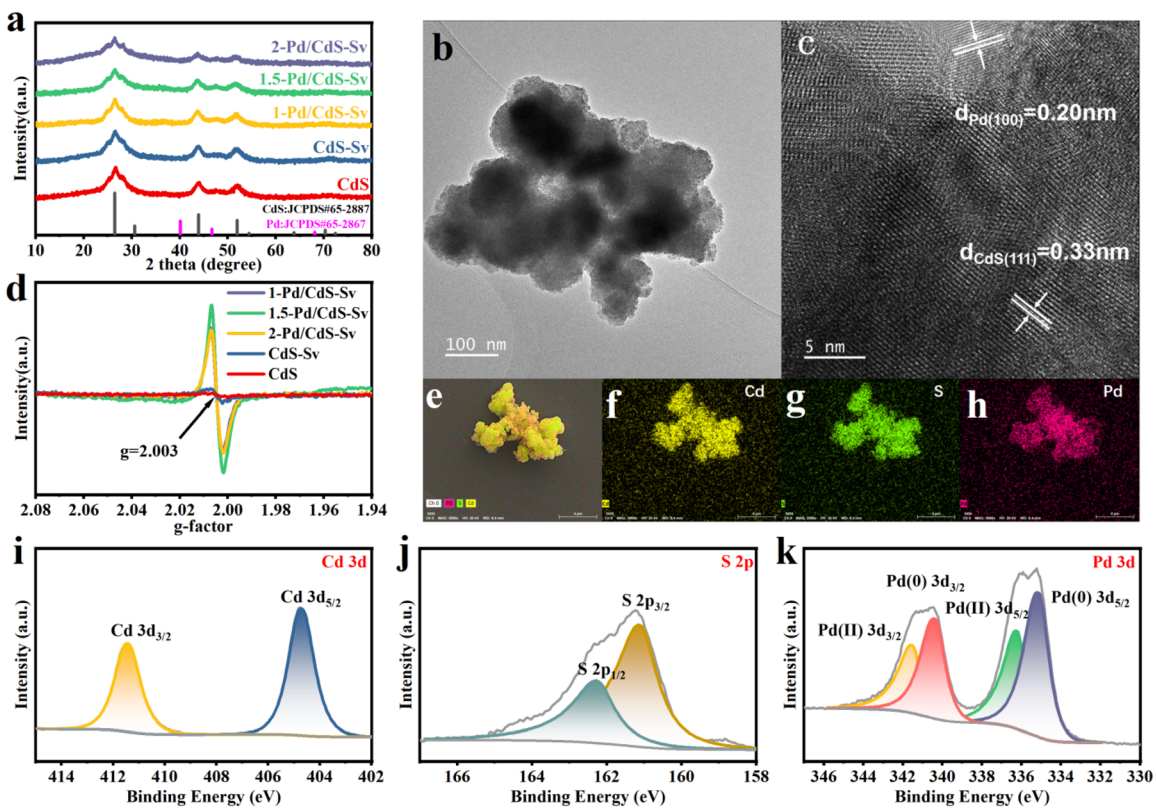

Fig. 1 (a) XRD patterns of CdS, CdS-Sv, 1-Pd/CdS-Sv, 1.5-Pd/CdS-Sv, and 2-Pd/CdS-Sv. (b and c) TEM and HRTEM images of 1.5-Pd/CdS-Sv. (d) EPR spectra of CdS, CdS-Sv, 1-Pd/CdS-Sv, 1.5-Pd/CdS-Sv, and 2-Pd/CdS-Sv. (e–h) EDS elemental mapping images of 1.5-Pd/CdS-Sv. (i) High-resolution Cd 3d XPS spectra, (j) high-resolution S 2p XPS spectra and (k) high-resolution Pd 3d XPS spectra of 1.5-Pd/CdS-Sv.

spacing of 0.20 nm was attributed to the (100) plane of Pd.[28] The elemental mapping of 1.5-Pd/CdS-Sv (Fig. 1e–h) showed a uniform distribution of Pd, Cd, and S elements, demonstrating the presence of metallic Pd. The XPS survey spectra (Fig. 1i–k) also confirmed the presence of Cd, S, and Pd in 1.5-Pd/CdS-Sv,[23,29] agreeing with the elemental mapping results. In addition, a signal with a *g* factor of 2.003 was observed for CdS-Sv in the electron paramagnetic resonance (EPR) spectra, indicating the presence of S vacancies (Fig. 1d).[30] More importantly, the enhanced EPR signal of *x*-Pd/CdS-Sv suggests that the addition of Pd led to an increase in the concentration of S vacancies.

Photocatalytic performance for CO_2 reduction

The performance of the synthesized samples for gas-phase CO_2 photoreduction was evaluated under light irradiation with a 300 W xenon lamp. Pristine CdS mainly produced CO at a rate of 16.9 μmol g^{-1} h^{-1} with a negligible amount of CH_4, as shown in Fig. 2a. In contrast, the C_2H_4 evolution rate of CdS-Sv slightly increased to 1.4 μmol g^{-1} h^{-1} due to the presence of S-vacancies, but the production of CO was still dominant with a high rate of 18.0 μmol g^{-1} h^{-1}. The introduction of Pd brought about a significant increase in the C_2H_4 yield on CdS-Sv but a decrease in the CO yield. From 1-Pd/CdS-Sv to 2-Pd/CdS-Sv, the C_2H_4 yield initially increased and then decreased. Among them, 1.5-Pd/CdS-Sv reached the maximum C_2H_4 evolution rate of 14.2 μmol g^{-1} h^{-1}, which was 158 and 10.1 times higher than that of pristine CdS and CdS-Sv, respectively. Accordingly, the selectivity of C_2H_4 was significantly improved from 2.1% (CdS) to nearly 81.6% (1.5-Pd/CdS-Sv). In addition, the CO_2 photoreduction activity of 1.5-Pd/CdS-Sv under UV-visible irradiation showed a negligible decrease after three cycles of irradiation for nine hours (Fig. 2b). Notably, the apparent quantum yield (AQY) for the photocatalytic CO_2 reduction reaction on 1.5-Pd/CdS-Sv was determined using different monochromatic lights (Fig. S7). The highest AQY reached 0.94%, and the AQY values were proportional to the wavelength-dependent light absorption capacity, further demonstrating that the CO_2 reduction process in this work is dominated by the photocatalytic reaction initiated by light absorption and excitation. The crystal structure (XRD) and elemental valence (XPS) (Fig. S2a–d) of 1.5-Pd/CdS-Sv before and after the reaction were almost the same, indicative of satisfactory photostability. Moreover, compared with most previously reported photocatalysts under similar conditions, 1.5-Pd/CdS-Sv performed among the best for the photoreduction of CO_2 to C_2H_4, with the top-level yield and selectivity (Fig. 2c and Table S1). Furthermore, control experiments performed under different conditions (Fig. 2d) ascertained that the obtained products indeed resulted from the reaction of CO_2 and H_2O.

Optical and photoelectrochemical properties

To further unravel the influence of Pd incorporated with CdS-Sv on CO_2 photoreduction, several optical and

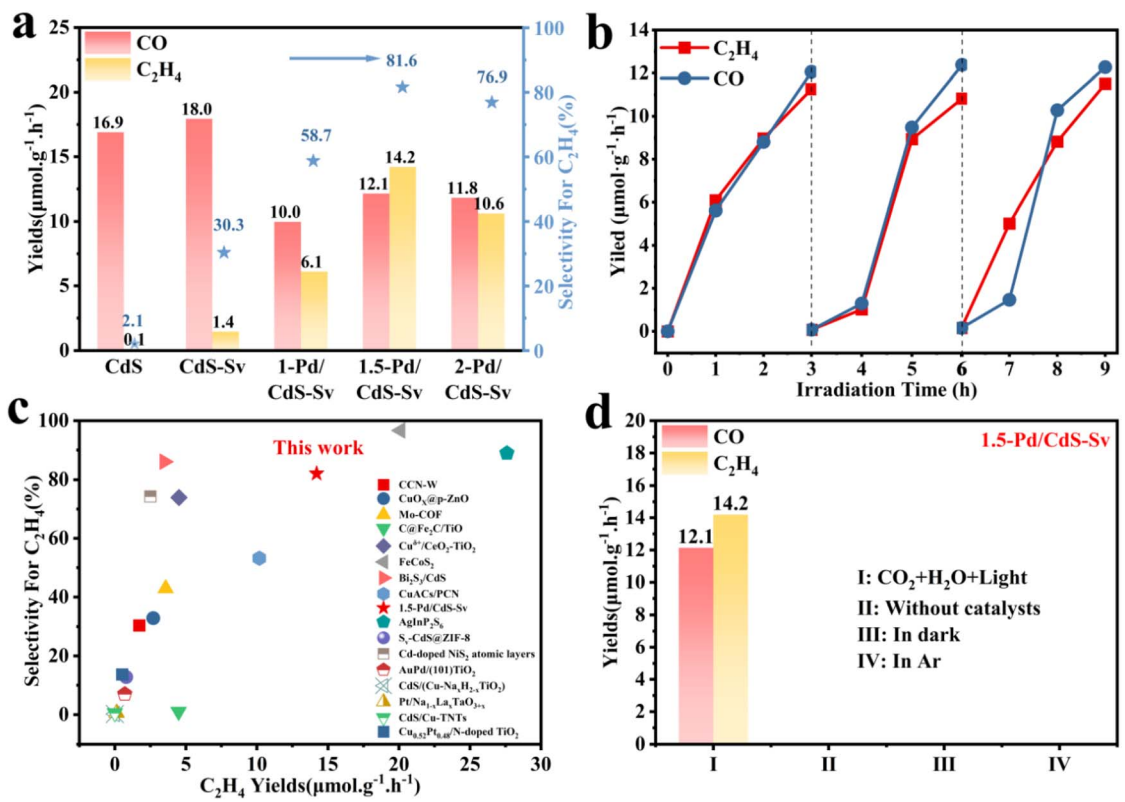

Fig. 2 (a) The photocatalytic CO_2 reduction performance of CdS, CdS-Sv, 1-Pd/CdS-Sv, 1.5-Pd/CdS-Sv, and 2-Pd/CdS-Sv. (b) Cycle stability test for nine hours of 1.5-Pd/CdS-Sv. (c) Comparison of selectivity and the product evolution rate of C_2H_4 with previously reported photocatalysts. (d) Photocatalytic CO_2 reduction performance of 1.5-Pd/CdS-Sv under different conditions.

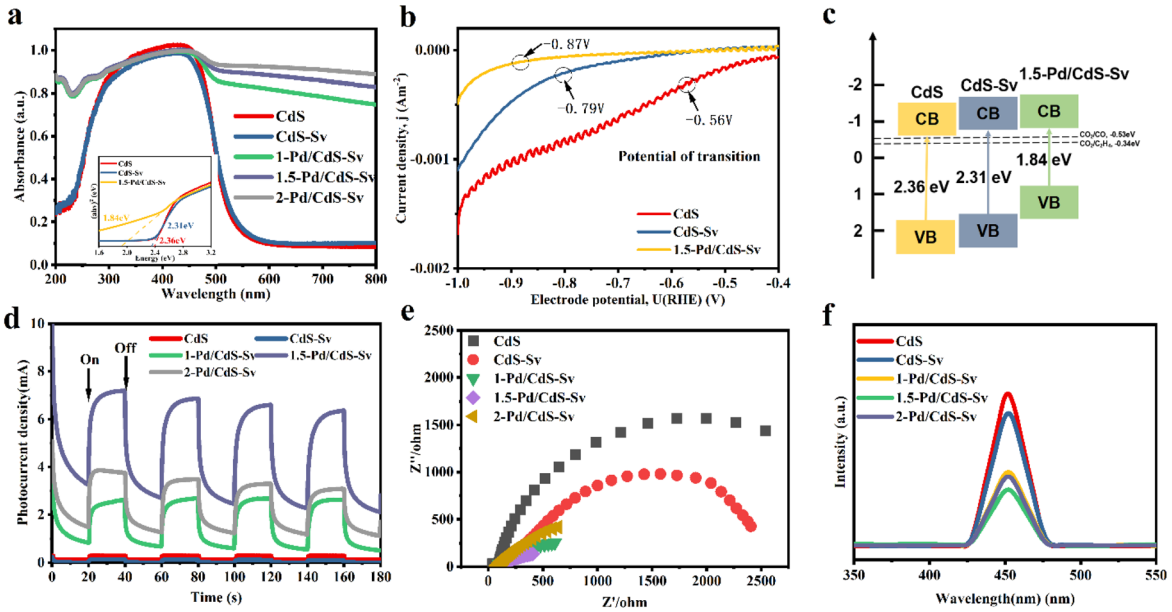

Fig. 3 (a) UV-vis diffuse reflectance spectrum of CdS, CdS-Sv, 1-Pd/CdS-Sv, 1.5-Pd/CdS-Sv, and 2-Pd/CdS-Sv; inset: the estimated band gap values for CdS, CdS-Sv, and 1.5-Pd/CdS-Sv are approximately 2.36 eV, 2.31 eV, and 1.84 eV, respectively. (b) Chopped photocurrents for CdS, CdS-Sv, and 1.5-Pd/CdS-Sv. (c) Band structure alignments with respect to the redox potentials at pH = 7 of CdS, CdS-Sv and 1.5-Pd/CdS-Sv. (d) Transient photocurrent density, (e) electrochemical impedance and (f) steady-state PL spectrum of CdS, CdS-Sv, 1-Pd/CdS-Sv, 1.5-Pd/CdS-Sv, and 2-Pd/CdS-Sv.

photoelectrochemical measurements were performed. As shown in Fig. 3a, the absorption edges of CdS and CdS-Sv were almost unchanged. However, for *x*-Pd/CdS-Sv, the absorption edge extended significantly toward 500–800 nm after the introduction of Pd. The absorption intensity was enhanced with the increase of Pd content. According to the density functional theoretical (DFT) calculations (Fig. S6), the band gap of the photocatalysts is narrowed after introducing S-vacancies and Pd atoms, and a distinctly empty mid-gap state is detected below the conduction band, which corresponds to the extended absorption of 500–800 nm. For 1.5-Pd/CdS-Sv, the band gap was shortened from 2.31 to 1.84 eV compared to CdS-Sv according to the Tauc plots (Fig. 3a inset) after Pd incorporation. The flat band potentials, determined from the potential at which the photocurrent changes sign (as shown in Fig. 3b), were measured to be −0.56 V, −0.79 V, and −0.87 V *vs.* RHE, respectively. Given the n-type semiconducting nature of CdS and the established equivalence between chopped photocurrent and flat band positions under minimal band bending conditions, these potentials approximate its conduction band minimum (CBM) energies. Thus, the CBM positions were established at −0.56 eV, −0.79 eV, and −0.87 eV *vs.* RHE for CdS, CdS-Sv, and 1.5-Pd/CdS-Sv. These energetically downshifted CBMs align with the predicted band structure modulations at pH 7 in Fig. 3c. Meanwhile, the transient photocurrent response was low on CdS and CdS-Sv. In sharp contrast, it significantly increased on *x*-Pd/CdS-Sv (Fig. 3d), indicating that introducing Pd clusters greatly enhanced the photo-electron density under light illumination. Benefiting from this, the *x*-Pd/CdS-Sv system presented a much lower electrochemical impedance (Fig. 3e). Compared to that of CdS-Sv, the lower PL emission intensity of *x*-Pd/CdS-Sv (Fig. 3f) further suggested that the carrier recombination rate has been effectively prohibited. In short, the above results demonstrate that introducing Pd is beneficial to the photocatalytic properties of CdS-Sv.

CO_2 reduction mechanism

In situ Fourier transform infrared spectroscopy (FTIR) measurements were utilized to analyze the reaction intermediates during CO_2 conversion on CdS-Sv and 1.5-Pd/CdS-Sv. As shown in Fig. 4a and b, the bands near 1310, 1370, 1480, and 1508 cm^{-1} confirmed the presence of CO_3^{2-},[31,32] which was the common intermediate for the adsorption of CO_2. Meanwhile, the characteristic peak near 1650 cm^{-1} on CdS-Sv could be attributed to *COOH,[33,34] a key intermediate in the reduction of CO_2 to hydrocarbons. The peak intensities at 1260, 1236, and 1108 cm^{-1} were respectively ascribed to the *ν(C–OH) and *CH groups. Compared to 1.5-Pd/CdS-Sv, CdS-Sv delivered the stronger peak intensities of *CO (1960 and 2060 cm^{-1}) and CO gas (2150 cm^{-1}), reflecting the fact that CdS-Sv mainly produces CO.[35] The negative signal peak around 1660 cm^{-1} was ascribed to the bending vibration of H–O–H in H_2O, indicative of water dissociation during the reaction.[36] It was significantly heightened on 1.5-Pd/CdS-Sv compared to CdS-Sv, demonstrating that the incorporation of Pd substantially facilitated water dissociation and thereby supplied *H, which are necessary for the subsequent hydrogenation of *CO.[34] As noted on 1.5-Pd/CdS-Sv, the distinct peaks at 1050 and 1740 cm^{-1} belonged to the *CHO groups,[37,38] which indicated the process of *CO protonation. More importantly, the band at 1357 cm^{-1} corresponded to the stretching mode of the hydrogenated dibasic intermediate *CHOCHO. This finding strongly supported the hypothesis that

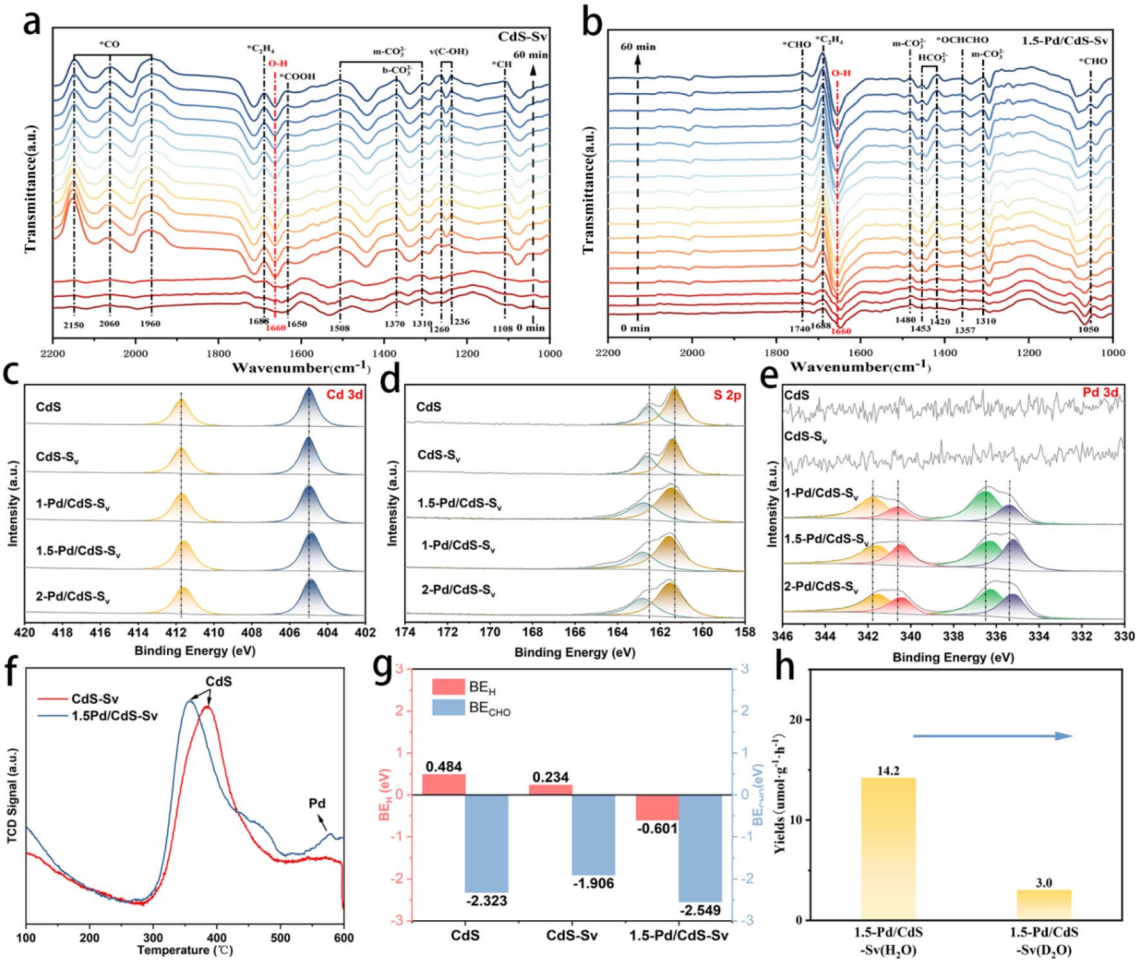

Fig. 4 Room temperature *in situ* diffuse reflectance infrared Fourier transform spectra of (a) CdS-Sv and (b) 1.5-Pd/CdS-Sv systems for the detection of intermediates during CO_2 photoreduction. (c) High-resolution Cd 3d XPS spectra, (d) high-resolution S 2p XPS spectra and (e) high-resolution Pd 3d XPS spectra of CdS, CdS-Sv, 1-Pd/CdS-Sv, 1.5-Pd/CdS-Sv, and 2-Pd/CdS-Sv. (f) CO-TPD of CdS-Sv and 1.5-Pd/CdS-Sv. (g) The binding energy diagram of *H and *CHO for different catalyst models. (h) Product evolution rates of C_2H_4 under H_2O or D_2O conditions of 1.5-Pd/CdS-Sv.

the system proceeded the C–C coupling *via* *CHO–CHO rather than *CO–CO. It is noteworthy that the *CHOCHO intermediate generally turns into C_2H_4 in the following hydrogenation process. Conformably, 1.5-Pd/CdS-Sv clearly showed the band at 1688 cm^{-1} attributed to the $*C_2H_4$ moiety,[39] providing solid evidence for the photoreduction of CO_2 to C_2H_4. Based on the *in situ* FTIR analysis, Fig. S3 depicts the possible reaction pathways for the reduction of CO_2 to CO and C_2H_4 in the 1.5-Pd/CdS-Sv system.

XPS was conducted to further analyze the role of S vacancies and Pd (Fig. 4c–e). The binding energy of Cd 3d in CdS-Sv was shifted negatively by 0.1 eV in comparison with that of CdS, demonstrating that Cd atoms gather electrons due to the presence of S vacancies. Meanwhile, the binding energy of Pd 3d shifted to a lower value with the increase of Pd content. These results suggest that the Pd and Cd atoms at the microinterface may have gathered more electrons, inducing the formation of Pd–Cd charge-asymmetrical metal pair sites. To further determine the actual active sites of 1.5-Pd/CdS-Sv during CO_2 photoreduction, CO temperature-programmed desorption (TPD) was performed for the CdS-Sv and 1.5-Pd/CdS-Sv systems. As shown in Fig. 4f and Tables S2 and S3, the desorption at 350–385 °C on CdS-Sv and 1.5-Pd/CdS-Sv was due to the CO desorption from CdS, and that at 578.5 °C on 1.5-Pd/CdS-Sv was ascribed to the desorption from Pd.[40] These results suggest that both CdS and Pd act as adsorption sites for CO. In addition, the lowest binding energies of *H and *CHO on 1.5-Pd/CdS-Sv imply that the anchoring effect of Pd facilitated the conversion of *CO to *CHO through the protonation process (Fig. 4g), which was consistent with the *in situ* FTIR results. In addition, we also performed controlled experiments of CO_2 photoreduction with D_2O replacing H_2O in the 1.5-Pd/CdS-Sv system (Fig. 4h). It should be noted that the rate of C_2H_4 evolution on 1.5-Pd/CdS-Sv was greatly reduced owing to the sluggish transfer of D, which confirmed that Pd may be an additional site for hydrolysis dissociation, thus providing more *H. This promoted the hydrogenation of the *CO intermediate to form *CHO and $*C_2H_4$. Contact angle tests also showed that the introduction of Pd greatly increased the hydrophilicity of 1.5-Pd/CdS-Sv (Fig.

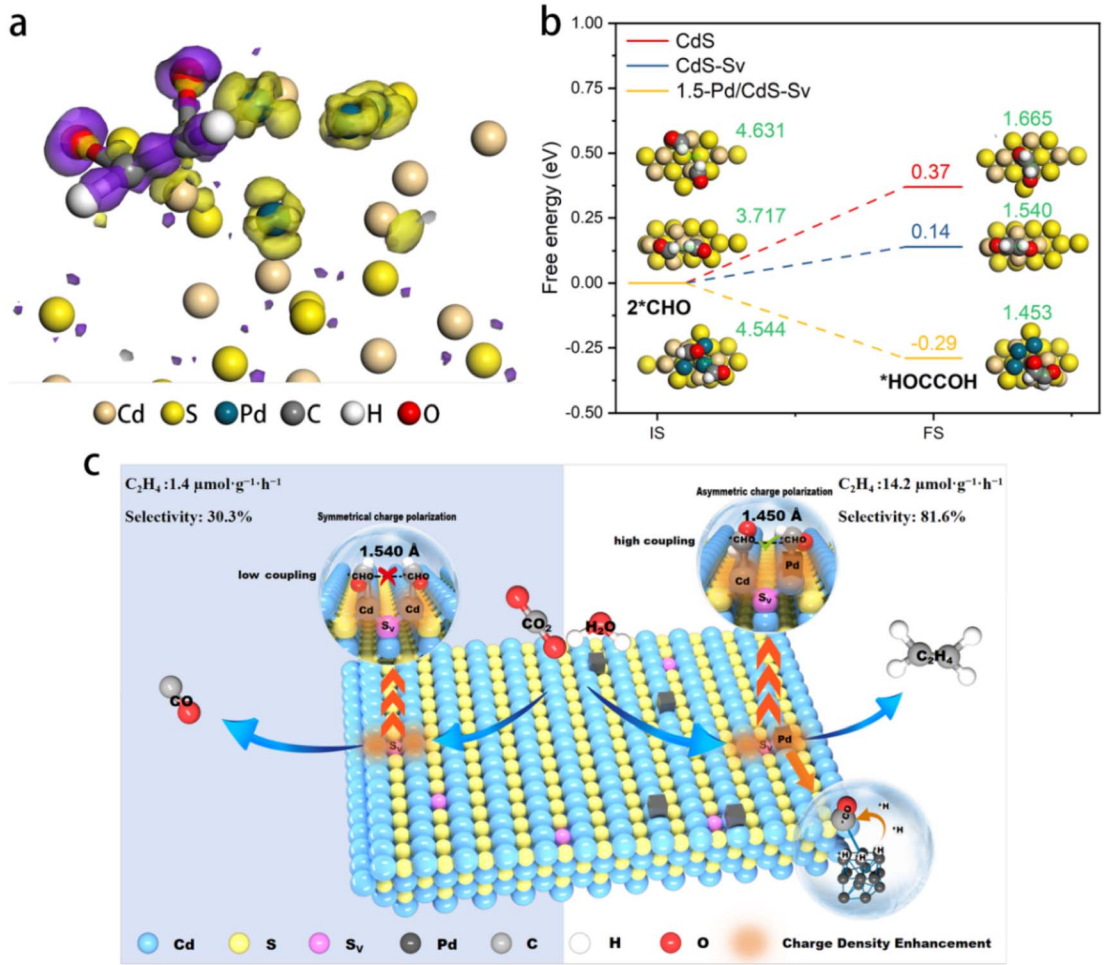

Fig. 5 (a) The charge density distribution of the *CHOCHO intermediate in 1.5-Pd/CdS-Sv (charge depletion and accumulation are labeled in yellow and purple, respectively). (b) The C–C atomic distances of the *CHOCHO intermediate and the Gibbs free energy diagrams of *CHO coupling to the *CHOCHO intermediate on CdS, CdS-Sv and 1.5-Pd/CdS-Sv systems. The "*" represents adsorption on the substrate. (c) The reaction mechanism for photocatalytic conversion of CO_2 to C_2H_4.

S4a–d), which seems to explain the enhanced water dissociation for 1.5-Pd/CdS-Sv.

Based on the above analysis, we also performed charge density difference calculations of the adsorbed *CHOCHO intermediates. As shown in Fig. 5a, electrons flowed from Pd and Cd atoms to the *CHOCHO intermediates around the S vacancy, which was a prerequisite for C–C coupling. This result indicated that the Pd and Cd atoms in 1.5-Pd/CdS-Sv acted as dual active sites to adsorb *CHO intermediates thanks to the asymmetric charge distribution. In other words, after the construction of the S vacancies and anchoring by Pd, the Cd–Cd site changes to the Cd–Pd pair site, which realizes the tight adsorption of *CHO intermediates and helps facilitate the C–C coupling step. In order to further investigate how 1.5-Pd/CdS-Sv promotes the C–C coupling of the dual *CHO intermediates, we further investigated the C–C atomic distances of the different species (*CO and *CHO) coupled on the three samples on the basis of the *in situ* FTIR spectra. As shown in Fig. S5, the C–C atomic distances of *COCO intermediates after *CO coupling were 2.419 Å, 3.629 Å, and 3.508 Å on the three models of CdS, CdS-Sv and 1.5-Pd/CdS-Sv, respectively, which were not in accordance with the theoretical distance of 1.330 Å in the C_2H_4 molecule. Compared with *CO dimerization, the C–C atomic distances of *CHOCHO intermediates became 1.665 Å, 1.540 Å, and 1.453 Å, respectively, after *CHO coupling (Fig. 5b). Most importantly, the Gibbs free energies of *CHO coupled to *CHOCHO were 0.37 eV, 0.14 eV, and −0.29 eV, respectively. The C–C coupling process could occur spontaneously only on Pd–Cd pair sites, which explained why CO_2 was more readily and selectively reduced to C_2H_4 on 1.5-Pd/CdS-Sv. These results also suggest that C–C coupling may be more favorable in the photoreduction of CO_2 to C_2H_4 *via* *CHO–CHO than *CO–CO coupling, which matches the results of *in situ* FTIR spectroscopy. The possible catalytic mechanism is shown in Fig. 5c.

Conclusions

In summary, we have designed and constructed Pd-based charge-asymmetrical metal pair sites that effectively perform *CHO–CHO coupling for the highly selective photoreduction of CO_2 to C_2H_4. With 1.5-Pd/CdS-Sv as a prototype, XPS spectroscopy and charge-density difference calculations confirmed that

electrons accumulate on Cd and Pd atoms to form Pd–Cd charge-asymmetrical metal pair sites, which were conducive to C–C coupling. Moreover, Pd promoted water dissociation to provide sufficient *H, promoting the conversion of *CO to *CHO and thus greatly facilitating *CHO–*CHO coupling with the obviously lowered energy barrier from 0.37 to −0.29 eV. As a result, the C_2H_4 evolution rate of 1.5-Pd/CdS-Sv was about 14.2 μmol g^{-1} h^{-1} with a selectivity of up to 81.6%, superior to most of the previously reported photocatalysts used under similar conditions. The work provides new perspectives to achieve highly selective CO_2 photoreduction to C_2 products by engineering charge-asymmetrical metal pair sites.

Author contributions

Writing – review & editing, Yuanming Zhang, Yi Zhu, and Qingsheng Gao; funding acquisition, Yi Zhu and Qingsheng Gao; project administration, Yi Zhu and Qingsheng Gao; data curation, Zhijie Pan, Wenbin Liao and Wenbiao Zhang; investigation, Zhijie Pan, Wenbin Liao and Wenbiao Zhang; validation, Mingyao Zhao and Xionghui Fu; visualization, Qun Liao.

Conflicts of interest

The authors declare no competing financial interest.

Data availability

The authors declare that the data supporting the findings of this study are available in the paper and its supporting information (SI). Supplementary information: experimental results—including XRD, SEM/TEM, XPS, gas chromatography, UV-vis, transient photocurrent, EIS, *in situ* IR, and contact angle measurements—as well as comprehensive methodological details on materials synthesis, reagents, and characterization protocols (*e.g.*, CO_2 reduction testing, photoelectrochemical measurements, apparent quantum yield determination, and theoretical calculations); all supporting references are cited (ref. 17 in the Supporting Information). is available. See DOI: **https://doi.org/10.1039/d5sc05310b**.

Acknowledgements

This work was supported by the Natural Science Foundation of Guangdong Province (2021A1515010390); the National Natural Science Foundation of China (22175077), the Innovation Team Project in Guangdong Colleges and Universities (2021KCXTD009), and the Fundamental Research Funds for the Central Universities (21621401 and 21623103). We thank Dr Xiang Yu, from the Analytical and Testing Center, Jinan University, Guangzhou 510632, P. R. China, for providing TEM and EDS technical support to carry out this research.

Notes and references

1 Y. Wu, Q. Chen, J. Zhu, K. Zheng, M. Wu, M. Fan, W. Yan, J. Hu, J. Zhu and Y. Pan, Selective CO_2-to-C_2H_4 Photoconversion Enabled by Oxygen-Mediated Triatomic Sites in Partially Oxidized Bimetallic Sulfide, *Angew. Chem., Int. Ed.*, 2023, **135**, e202301075.

2 C. Feng, M. Hu, S. Zuo, J. Luo, P. Castaño, Y. Ren, M. Rueping and H. Zhang, Ru-OV Site-Mediated Product Selectivity Switch for Overall Photocatalytic CO_2 Reduction, *Adv. Mater.*, 2025, **37**, 2411813.

3 P.-P. Yang, X.-L. Zhang, F.-Y. Gao, Y.-R. Zheng, Z.-Z. Niu, X. Yu, R. Liu, Z.-Z. Wu, S. Qin, L.-P. Chi, Y. Duan, T. Ma, X.-S. Zheng, J.-F. Zhu, H.-J. Wang, M.-R. Gao and S.-H. Yu, Protecting copper oxidation state *via* intermediate confinement for selective CO_2 electroreduction to C_{2+} fuels, *J. Am. Chem. Soc.*, 2020, **142**, 6400–6408.

4 F. Wen, L. Song, X. Lv, S. Wang, G. Zheng and Q. Han, Atomically Dispersed Cobalt on Quinacridone-Embedded Donor-Acceptor Conjugated Mesoporous Polymer for Efficient Photocatalytic CO_2-to-Syngas, *Appl. Catal., B*, 2024, **365**, 124929.

5 J. Fang, C. Zhu, L. Fang, Y. Chen, H. Hu, Y. Wu, Q. Chen and J. Mao, Efficient charge relay steering in Pd nanoparticles coupled with the heterojunction for boosting CO_2 photoreduction to C_2H_6, *Sci. China Mater.*, 2024, **67**, 2949–2956.

6 J. Fang, C. Zhu, H. Hu, J. Li, L. Li, H. Zhu and J. Mao, Progress of photocatalytic CO_2 reduction toward multi-carbon products, *Sci. China: Chem.*, 2024, **67**, 3994–4013.

7 S. Chakraborty, R. Das, M. Riyaz, K. Das, A. K. Singh, D. Bagchi, C. P. Vinod and S. C. Peter, Wurtzite $CuGaS_2$ with an In-Situ-Formed CuO Layer Photocatalyzes CO_2 Conversion to Ethylene with High Selectivity, *Angew. Chem., Int. Ed.*, 2023, **62**, e202216613.

8 K.-X. Chen, Y. Wang, Y.-Q. Dong, Z.-H. Zhao, Y. Zang, G.-L. Zhang, Y. Liu and F.-M. Zhang, Theoretical Design of Dual-Site Metallo-Covalent Organic Frameworks for Efficient CO_2 Photoreduction into C_2H_4, *Appl. Catal., B*, 2024, **365**, 124933.

9 Z. Wang, J. Zhu, X. Zu, Y. Wu, S. Shang, P. Ling, P. Qiao, C. Liu, J. Hu and Y. Pan, Selective CO_2 Photoreduction to CH_4 *via* $Pd^{\delta+}$-Assisted Hydrodeoxygenation over CeO_2 Nanosheets, *Angew. Chem., Int. Ed.*, 2022, **61**, e202203249.

10 S. Xie, Q. Zhang, G. Liu and Y. Wang, Photocatalytic and photoelectrocatalytic reduction of CO_2 using heterogeneous catalysts with controlled nanostructures, *Chem. Commun.*, 2016, **52**, 35–59.

11 S. Dou, J. Song, S. Xi, Y. Du, J. Wang, Z. F. Huang, Z. J. Xu and X. Wang, Boosting electrochemical CO_2 reduction on metal-organic frameworks *via* ligand doping, *Angew. Chem., Int. Ed.*, 2019, **58**, 4041–4045.

12 A. Zhang, R. He, H. Li, Y. Chen, T. Kong, K. Li, H. Ju, J. Zhu, W. Zhu and J. Zeng, Nickel doping in atomically thin tin disulfide nanosheets enables highly efficient CO_2 reduction, *Angew. Chem., Int. Ed.*, 2018, **130**, 11120–11124.

13 Y. Ji and Y. Luo, New mechanism for photocatalytic reduction of CO_2 on the anatase TiO_2 (101) surface: the essential role of oxygen vacancy, *J. Am. Chem. Soc.*, 2016, **138**, 15896–15902.

14 M.-y. Liu, R.-T. Guo, C. Liu, H.-f. Cui, H.-w. Zhu and W.-G. Pan, Research progress in photocatalytic reduction of CO_2 based on metal nanocluster materials, *J. Mater. Chem.*, 2024, **12**, 32665–32688.

15 L. Cheng, X. Yue, L. Wang, D. Zhang, P. Zhang, J. Fan and Q. Xiang, Dual-single-atom tailoring with bifunctional integration for high-performance CO_2 photoreduction, *Adv. Mater.*, 2021, **33**, 2105135.

16 X. Shang, G. Li, R. Wang, T. Xie, J. Ding and Q. Zhong, Precision loading of Pd on Cu species for highly selective CO2 photoreduction to methanol, *Chem. Eng. J.*, 2023, **456**, 140805.

17 Y. Wu, Q. Hu, Q. Chen, X. Jiao and Y. Xie, Fundamentals and challenges of engineering charge polarized active sites for CO_2 photoreduction toward C_2 products, *Acc. Chem. Res.*, 2023, **56**, 2500–2513.

18 K. Das, R. Das, M. Riyaz, A. Parui, D. Bagchi, A. K. Singh, A. K. Singh, C. P. Vinod and S. C. Peter, Intrinsic Charge Polarization in $Bi_{19}S_{27}Cl_3$ Nanorods Promotes Selective C-C Coupling Reaction during Photoreduction of CO_2 to Ethanol, *Adv. Mater.*, 2023, **35**, 2205994.

19 H. Shi, H. Wang, Y. Zhou, J. Li, P. Zhai, X. Li, G. G. Gurzadyan, J. Hou, H. Yang and X. Guo, Atomically dispersed indium-copper dual-metal active sites promoting C-C coupling for CO_2 photoreduction to ethanol, *Angew. Chem., Int. Ed.*, 2022, **134**, e202208904.

20 J. Ji, R. Li, H. Zhang, Y. Duan, Q. Liu, H. Wang and Z. Shen, Highly selective photocatalytic reduction of CO_2 to ethane over Au-O-Ce sites at micro-interface, *Appl. Catal., B*, 2023, **321**, 122020.

21 W. Luo, X. Nie, M. J. Janik and A. Asthagiri, Facet dependence of CO_2 reduction paths on Cu electrodes, *ACS Catal.*, 2016, **6**, 219–229.

22 W. MacSwain, H. Lin, Z.-J. Li, S. Li, C. Chu, L. Dube, O. Chen, G. Leem and W. Zheng, Facilitated electron transfer by Mn dopants in 1-dimensional CdS nanorods for enhanced photocatalytic hydrogen generation, *J. Mater. Chem.*, 2023, **11**, 7066–7076.

23 F. Tian, H. Zhang, S. Liu, T. Wu, J. Yu, D. Wang, X. Jin and C. Peng, Visible-light-driven CO_2 reduction to ethylene on CdS: Enabled by structural relaxation-induced intermediate dimerization and enhanced by ZIF-8 coating, *Appl. Catal., B*, 2021, **285**, 119834.

24 X.-L. Ma, W.-X. Shi, S. Guo, Q.-P. Zhao, W. Lin, T.-B. Lu and Z.-M. Zhang, Gram-Scale Green-Synthesis of High Purity Pinacols and Amides by Continuous Tandem Photocatalysis *via* a Negative Carbon Emission Process, *Adv. Mater.*, 2025, 2506133.

25 S. Fu, S. Yao, S. Guo, G.-C. Guo, W. Yuan, T.-B. Lu and Z.-M. Zhang, Feeding Carbonylation with CO2 *via* the Synergy of Single-Site/Nanocluster Catalysts in a Photosensitizing MOF, *J. Am. Chem. Soc.*, 2021, **143**, 20792–20801.

26 Y. Zhu, C. Gao, S. Bai, S. Chen, R. Long, L. Song, Z. Li and Y. Xiong, Hydriding Pd cocatalysts: An approach to giant enhancement on photocatalytic CO_2 reduction into CH_4, *Nano Res.*, 2017, **10**, 3396–3406.

27 Y. Mao, M. Zhang, G. Zhai, S. Si, D. Liu, K. Song, Y. Liu, Z. Wang, Z. Zheng and P. Wang, Asymmetric Cu (I)-W Dual-Atomic Sites Enable C-C Coupling for Selective Photocatalytic CO_2 Reduction to C_2H_4, *Adv. Sci.*, 2024, **11**, 2401933.

28 Q. Chen, W. Mo, G. Yang, S. Zhong, H. Lin, J. Chen and S. Bai, Significantly enhanced photocatalytic CO_2 reduction by surface amorphization of cocatalysts, *Small*, 2021, **17**, 2102105.

29 P. Liu, Z. Huang, X. Gao, X. Hong, J. Zhu, G. Wang, Y. Wu, J. Zeng and X. Zheng, Synergy between palladium single atoms and nanoparticles *via* hydrogen spillover for enhancing CO_2 photoreduction to CH_4, *Adv. Mater.*, 2022, **34**, 2200057.

30 Y. Zhang, H. Huang, L. Wang, X. Zhang, Z. Zhu, J. Wang, W. Yu and Y. Zhang, Cooperation of congenital and acquisitus sulfur vacancy for excellent photocatalytic hydrogen peroxide evolution of CdS nanorods from air, *Chem. Eng. J.*, 2023, **454**, 140420.

31 W. Xie, K. Li, X. H. Liu, X. Zhang and H. Huang, P-Mediated Cu–N4 Sites in Carbon Nitride Realizing CO_2 Photoreduction to C_2H_4 with Selectivity Modulation, *Adv. Mater.*, 2023, **35**, 2208132.

32 K. Wang, J. Fu and Y. Zheng, Insights into photocatalytic CO_2 reduction on C_3N_4: Strategy of simultaneous B, K co-doping and enhancement by N vacancies, *Appl. Catal., B*, 2019, **254**, 270–282.

33 Y. Ma, Y. Zhang, G. Xie, Z. Huang, L. Peng, C. Yu, X. Xie, S. Qu and N. Zhang, Isolated Cu sites in CdS hollow nanocubes with doping-location-dependent performance for photocatalytic CO_2 reduction, *ACS Catal.*, 2024, **14**, 1468–1479.

34 J. Hao, D. Yang, J. Wu, B. Ni, L. Wei, Q. Xu, Y. Min and H. Li, Utilizing new metal phase nanocomposites deep photocatalytic conversion of CO_2 to C_2H_4, *Chem. Eng. J.*, 2021, **423**, 130190.

35 W. Lyu, Y. Liu, D. Chen, F. Wang and Y. Li, Engineering the electron localization of metal sites on nanosheets assembled periodic macropores for CO_2 photoreduction, *Nat. Commun.*, 2024, **15**, 10589.

36 S. Yin, X. Zhao, E. Jiang, Y. Yan, P. Zhou and P. Huo, Boosting water decomposition by sulfur vacancies for efficient CO_2 photoreduction, *Energy Environ. Sci.*, 2022, **15**, 1556–1562.

37 K. Wang, Q. Li, X. Chen, Z. Li, Y.-F. Yang, T.-S. Zhang, H.-M. Shen, Q. Wang, B. Wang and Y. Zhang, Porous organic polymers with shiftable active Co (II) sites for photocatalytic reduction of CO_2 to C_2H_4, *Appl. Catal., B*, 2025, **362**, 124765.

38 R. Xu, D.-H. Si, S.-S. Zhao, Q.-J. Wu, X.-S. Wang, T.-F. Liu, H. Zhao, R. Cao and Y.-B. Huang, Tandem photocatalysis of CO_2 to C_2H_4 *via* a synergistic rhenium-(I) bipyridine/copper-porphyrinic triazine framework, *J. Am. Chem. Soc.*, 2023, **145**, 8261–8270.

39 N. Zhang, J. Lü and R. Cao, Photocatalytic CO_2–to–ethylene conversion over Bi_2S_3/CdS heterostructures constructed *via* facile cation exchange, *Research*, 2022, **2022**, 9805879.

40 J. Hulva, M. Meier, R. Bliem, Z. Jakub, F. Kraushofer, M. Schmid, U. Diebold, C. Franchini and G. S. Parkinson, Unraveling CO adsorption on model single-atom catalysts, *Science*, 2021, **371**, 375–379.